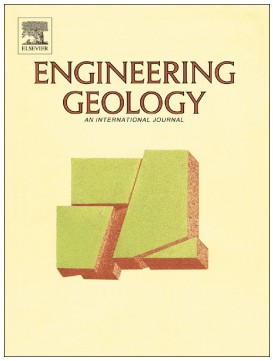

Geological hazard assessment of the coastal area of Rome (Central Italy) from multi-source data integration

Roberta Maffucci, Giancarlo Ciotoli, Andrea Pietrosante, Gian Paolo Cavinato, Salvatore Milli, Livio Ruggiero, Alessandra Sciarra, Sabina Bigi

PII: S0013-7952(22)00012-6

DOI: https://doi.org/10.1016/j.enggeo.2022.106527

Reference: ENGEO 106527

To appear in: *Engineering Geology*

Received date: 14 June 2021

Revised date: 25 October 2021

Accepted date: 7 January 2022

Please cite this article as: R. Maffucci, G. Ciotoli, A. Pietrosante, et al., Geological hazard assessment of the coastal area of Rome (Central Italy) from multi-source data integration, *Engineering Geology* (2021), https://doi.org/10.1016/j.enggeo.2022.106527

Geological hazard assessment of the coastal area of Rome (central Italy) from multi-source data integration

Roberta Maffucci[(1,4)], Giancarlo Ciotoli[(2,3)], Andrea Pietrosante[(2,4)], Gian Paolo Cavinato[(2)], Salvatore Milli[(1,2)], Livio Ruggiero[(3)], Alessandra Sciarra[(3)], Sabina Bigi[(1)]

(1) Dipartimento di Scienze della Terra, SAPIENZA Università di Roma, P. le Aldo Moro 5, 00185 Roma, Italy
(2) CNR-IGAG Istituto di Geologia Ambientale e Geoingegneria, Via Salaria km 29,300, 00015 Monterotondo (RM), Italy
(3) INGV - Istituto Nazionale di Geofisica e Vulcanologia, Sezione Roma1, Via di Vigna Murata 605, 00143 Roma, Italy
(4) Dipartimento di Scienze Umanistiche, della Comunicazione e del Turismo, Università degli Studi della Tuscia, Via S. Maria in Gradi, 4, 01100 Viterbo, Italy

Abstract

This work presents the first 3D geological model of the Rome coastal area that integrates available subsurface geological, stratigraphic and geophysical data with surface geochemical data obtained both from the literature and new surveys. The model provides new insights into the stratigraphic and tectonic setting of the area and the geological factors controlling both natural and human-induced gas emissions. This sector of the Italian Tyrrhenian margin has been historically affected by natural emissions of deep CO_2 and thermogenic CH_4, stored in permeable layers but with local migration to the surface along buried normal faults. In addition to natural processes, human activities can also cause leakage and serious health risks, such as the abrupt gas release in August, 2013, that was triggered by borehole drillings near the Rome international airport.

The presented 3D reconstruction unveils the link between faults, stratigraphy, lithology and the distribution of the soil gas anomalies. It provides information about the depth of the reservoir that can potentially trap endogenous gases, and the location and geometry of the main faults along which the gas migrates towards the surface. Furthermore, reconstruction

of the distribution and thickness of important clay layers better constrains the low permeable areas that prevent gas escape.

The 3D model, coupled with the geochemical information, can serve as a useful tool for the local administration to perform land-use planning and manage the local geological and degassing hazards that affect this highly urbanised area near Rome. Furthermore, we estimate that the large amount of CO_2 broadly released in the area also provides a contribution to the budget of natural greenhouse gases in the atmosphere.

Keywords

3D geological model

Soil gas

Active faults

Surface degassing

Geological hazards

Tiber delta

1. Introduction

The coastal area of Rome is located on the eastern margin of the Tyrrhenian Sea and develops along the Tiber river delta. The area has an extremely important cultural and environmental heritage, and in recent decades has undergone intensive urbanization due to its proximity to Rome and the presence of the “Leonardo da Vinci” International Airport (Fig. 1). The archaeological site of Ostia Antica, which was founded by King Ancus Marcius in the 620 BC and that served as the fluvial harbour for the city of Rome, is located in this area in a bend of the Tiber river (Fig. 1). In 42 BC, the Emperors Claudius and Trajan built a new harbour for Rome (called Portus), north of the Tiber mouth. Later, during the medieval period, Pope Gregorio IV established the fortified village of

"Gregoriopolis" (currently Ostia Antica village), in which is also present the renaissance "Castle of Giulio II" built by Pope Giulio II starting from 1483. To the south of Ostia Antica there is a large green area, Castel Fusano Pinewood Nature Reserve, which hosts the well-preserved remains of the Roman Via Severiana road and the Roman Villa della Palombara.

Due to such important cultural and environmental heritage, the expanding urban areas, and the presence of an international airport, the coastal area of Rome needs to be protected from numerous local geological hazards, such as flooding (Calenda et al. 2005), subsidence related to peat compaction (Del Ventisette et al., 2015), beach erosion (Lamberti et al., 2005) and salt-water intrusion (Capelli et al., 2007). In the last few years, accidental gas blowouts represent a new hazard caused by increasing urbanisation. This phenomenon can occur during shallow geotechnical drilling that allows the escape of CO_2 accumulated in pressurized aquifers, which are mostly located within the gravel layers of the Middle Pleistocene Ponte Galeria formation and confined underneath the shallow impermeable horizons of the Tiber delta stratigraphic succession. One well-documented example is a gas eruption that occurred close to the airport after the drilling of a borehole in August 2013 (Bigi et al., 2014; Sella et al., 2014; Carapezza et al., 2015; Ciotoli et al., 2013, 2016), while similar, less-well known accidents have occurred throughout the area (see Sella et al., 2014 with references therein).

In 2013, the first extensive and detailed soil gas and gas flux survey conducted in the Fiumicino-Isola Sacra area recorded very high soil gas anomalies of mantle CO_2 associated with thermogenic CH_4. Gas anomalies were mainly located in correspondence with active normal faults identified by new seismic reflection profiles acquired along the Tiber river (Bigi et al., 2014; Ciotoli et al., 2013; 2016). In this work we integrate results from a new geochemical survey with those already available (Ciotoli et al., 2016), with the goal of investigating the geological factors controlling the degassing processes. This was

achieved by creating the first multi-source 3D geological model of the area by integrating available surface (geological maps) and subsurface (boreholes, geological cross-sections and seismic reflection profiles) data from available CNR-IGAG databases and the literature. The model provides also new insight into the stratigraphic and tectonic setting of the area.

Soil gas distribution and anomalies are also interpreted and explained in light of the distribution of peat and organic clay layers, deposited during the last phase of the Tiber delta evolution.

The high CO_2 concentration and flux values measured within this urban area represent a relevant risk for human health in general and during construction-related human activities in particular, and thus gas distribution maps constitute an important tool for public administrations to delimit areas at risk of sudden degassing.

In addition, we quantify total CO_2 leakage rates and assess their potential impact on the atmospheric budget of greenhouse gases (GHG).

2. Geological setting

The coastal area west of Rome occupies a large portion of the Tiber delta plain, which extends along the central coastal sector of the Latium region (Tyrrhenian margin of central Italy) (Fig. 1). This sector of the Italian peninsula occurs along the eastern side of the Tyrrhenian Sea back-arc basin, a basin formed since the Upper Miocene as a consequence of back arc extensional tectonics associated with the progressive eastward migration of the west-directed Apennine subduction (see Carminati et al., 2012 and references therein). In this area, extensional tectonics was responsible for the generation of NW-SE and NE-SW normal faults that controlled the Plio-Quaternary volcanism of the area (Roman Magmatic Province; Acocella and Funiciello, 2006) and the development of

NNW-SSE-, NW-SE- and, subordinately, NE-SW-oriented sub-basins that are filled with syn-rift and post-rift clastic sediments and volcaniclastic deposits (Faccenna et al., 1994).

The investigated area is part of the extensional Roman Basin, which extends north and south of the Tiber river for about 135 km. The evolution of this basin started in the Late Pliocene and was accompanied by a continuous vertical tectonic uplift that was coeval with the volcanism of the area (Milli et al., 2016). These processes, together with the glacio-eustatic sea-level variations related to Quaternary climatic changes, controlled the basin's stratigraphic framework (Milli et al., 2016) and led to the creation of low rank depositional sequences (sensu Catuneanu et al., 2011) over 30 to 120 kyr time periods. These are stacked to form two composite high rank sequences: the Monte Mario Sequence (MMS: Lower Pleistocene) and the Ponte Galeria Sequence (PGS: Late Lower Pleistocene-Holocene) (Milli et al., 2013, 2016).

The study area is located between the present lower and upper Tiber delta plain (Fig. 1). The stratigraphic succession beneath this sector is characterized by three main units that are bounded by unconformity surfaces (Fig. 2). The lowermost stratigraphic unit, which consists of Lower Pleistocene (Emilian stage) shelf clay and silty clay with local intercalations of sandy layers is attributed to the Monte delle Piche formation (MDP) (Funiciello and Giordano, 2008). This unit forms part of the transgressive systems tract of the MMS (Milli et al., 2016). The middle stratigraphic unit consists of Middle Pleistocene fluvial and coastal gravels and sandy gravels with associated volcanoclastic deposits deriving from the Sabatini and Albani volcanic complexes; the latter outcrop to the north and south of the Tiber river. The deposits of this unit belong to the Ponte Galeria formation (PGL), which consists of low rank depositional sequences (from PG1 to PG4) that are part of the high rank Ponte Galeria Sequence (PGS) (Milli et al., 2016). The PGL developed during the late lowstand and the early transgressive systems tracts of the PGS. Its deposits, which are exposed in the eastern sector of the study area and are buried

westward, include sediments derived from carbonate to siliciclastic Meso-Cenozoic rocks and from Pleistocene volcanic complexes of the Roman Magmatic Province (Tentori et al., 2016).

In the Fiumicino area, the gravel deposits of the PGL formation locally form a gas pressurized confined aquifer (Carapezza et al., 2015; Sella et al., 2014). The uppermost unit that outcrops in the studied area belongs to the Upper-Pleistocene to Holocene Tiber River synthem (SFT) (Funiciello and Giordano, 2008); it constitutes a low rank still-evolving depositional sequence known in the literature as the Tiber Depositional Sequence (TDS – PG9) (Bellotti et al., 1995; Milli et al., 2013, 2016) (Fig. 2 and supplementary figure S1). The TDS is the last low rank sequence forming the PGS, developing during the highstand system tract of the PGS. It includes the sedimentary succession formed during the last glacial–interglacial cycle of the post-Tyrrhenian age. Its deposits reflect either the contribution of the major tributaries of the Tiber drainage basin or the modification that these sediments underwent in the coastal environment by hydraulic sorting and mixing with detritus derived from the recycling of coastal dune sands and altered volcaniclastic paleosols (Tentori et al., 2018). The deposits of the TDS show variable thicknesses (from 40 to 80 m) and a complex depositional architecture that records the transition from a wave-dominated estuary to a wave-dominated delta (Fig. S1). This evolution is characterized by: (i) valley incision and alluvial plain formation during the early lowstand systems tract (ELST); (ii) partial filling of the valley during the late lowstand systems tract (LLST); (iii) complete filling of the valley and rapid landward migration of barrier-lagoon-estuary systems during the transgressive systems tract (TST); and (iv) progradation of a wave-dominated delta during the highstand systems tract (HST). The lower boundary of this sequence is an erosional surface, which is carved into the underlying Lower–Middle Pleistocene deposits (Milli et al., 2013, 2016). In particular, during the landward migration of the barrier-lagoon-estuary depositional system of the TST, the area behind the lagoons

was transformed into a marshy environment filled with thick deposits of compressible peat and organic clay (Fig. S1).

Furthermore, below the present Tiber delta plain, westward dipping normal faults have been detected in recent seismic reflection profiles acquired along the Tiber river (Bigi et al., 2014) that cross the Isola Sacra and Fiumicino urban areas (Fig. 2). The fault planes offset the main basal unconformity surface of the TDS and the underlying deposits.

In this area, very high soil gas anomalies with mantle CO_2 have been detected (Bigi et al.; 2014; Ciotoli et al., 2016). This suggested that the detected faults may act as vertical migration pathways for large volumes of gas (Bigi et al., 2014).

3. Data and Methods

3.1. Soil gas sampling and analyses

In the summer of 2017, a total of 457 soil gas samples (blue dots in the supplementary figure S2) were collected over an area of about 70 km^2 (~ 7 samples/km^2) in the Ponte Galeria (215 samples) and Ostia Antica areas (242 samples), on the right and on left sides of the Tiber river, respectively (Fig. S2). This new dataset was compared, integrated and then reinterpreted with previous soil gas data (orange dots in figure S2) collected in the Fiumicino-Isola Sacra area (Ciotoli et al., 2016). Considering that the Tiber river constitutes an important break line that separates these three groups of samples, 60 samples located on the left bank of the Tiber river were merged, for statistical purposes, with the samples taken in the Ostia Antica area. Samples from these three geographically distinct areas were re-interpreted in the light of the results obtained by the new stratigraphic and structural analyses.

Carbon dioxide (CO_2), methane (CH_4), hydrogen (H_2) and oxygen (O_2) were analysed in the field using a portable gas analyzer (Draeger X-am 7000, accuracy <5%) connected to a sampling probe hand-pounded to a depth of about 80 cm in the unsaturated soil layer

(Ciotoli et al., 2016). Gas samples were also collected, stored and subsequently analysed in the Fluid Chemistry Laboratory of Sapienza University of Rome using a mass spectrometer (Varian Leak Detector) for helium (He) and two Fisons 8000-series bench gas chromatographs (accuracy ±1%) for permanent gases (CO_2, O_2+Ar, N_2), and the light hydrocarbon gases of methane (CH_4), ethane (C_2H_6) and propane (C_3H_8). CO_2 flux (φCO_2) measurements were also performed at the ground surface using an in-house developed closed-chamber system (0.2x0.2x0.1m) connected with a CO_2 non-dispersive infrared sensor (measurement range of 0-3000 ppmv, resolution of 1 ppm and accuracy of ±2%). Gas flux is calculated using the chamber's volume and surface area and by fitting a linear regression of the gas concentration (ppmv s^{-1}) increase in the chamber. The final flux value is expressed in g CO_2 m^{-2} d^{-1}.

Gas samples for molecular and isotopic analyses were also collected in different periods, from August 2013 to April 2018, at 13 visible vents (bubbles or dry emissions from soil; indicated as "V" in figure S2) and from soil gas at 11 sites (indicated as "s" in figure S2). The gas vents V11, V12, V13 and the soil gas from vent zone s11 were newly discovered during this field work, and thus they have been merged with the data from vents V1-10 Ciotoli et al. (2013, 2016) and re-discussed here.

Stable C and H isotope compositions of CH_4 and CO_2 were analysed using a Delta Plus XP IRMS coupled with a Thermo TRACE GC, a Thermo GC/C III interface and equipped with a Poraplot column at the Stable Isotope Laboratory of INGV Palermo. $^{13}C/^{12}C$ ratios are reported as $\delta^{13}C$ values (1 σ=0.1‰) against the VPDB standard and $^{2}H/^{1}H$ ratios are reported as $\delta^{2}H$ values (1σ=1‰) against the VSMOW standard. In this work, the entire soil gas dataset (including CO_2, CH_4, He and CO_2 flux values) is presented and compared by Exploratory Data Analysis (EDA), consisting of descriptive statistics and exploratory graphs used for data interpretation, discover data structure, and define outliers and anomalies linked to deep gas migration phenomena. In particular, histograms were used to

analyze and display the data distribution and the probability density curve type. Box-plots were used to compare the distribution of different datasets in the three studied areas. Normal Probability Plots (NPP) were used to graphically examine data distribution (normal or log-normal), to separate background from anomalous populations and thus define the anomaly “threshold” values used to construct classed-post maps. In addition, geospatial analysis techniques, including variogram analysis and modelling, were applied to examine spatial autocorrelation of the soil gas data. Kriging was used to construct maps of soil gas concentration.

3.2. Borehole analysis

In order to estimate the thickness and spatial distribution of peat and organic clay layers (hereafter POC) in the subsurface, we analysed data from 637 georeferenced boreholes, some from the CNR-IGAG (National Council of Italian Research) Urbisit database and others from literature (Bellotti et al. 1995, 2007; Ventriglia 2002; Di Bella et al., 2011; Salomon et al., 2012, 2020; Marra et al., 2013; Goiran et al., 2014; Milli et al., 2016; Sadori et al., 2016) (Supplementary figure S3). In our analyses, and in the subsequent interpolation of the POC thickness values, we only considered boreholes deeper than 30 meters to ensure that the thickest and most laterally continuous peat and organic clay horizons were intersected (Bellotti et al., 1995; Milli et al., 2016). The POC thicknesses reported in each borehole profile were interpolated using the Ordinary Kriging method which computes values at a given point using both distance of the known values and their spatial relationships to minimize mean square prediction error.

3.3. 3D Geological Modelling

During the last decades, the development of advanced geoscience software allows to represent the geology of subsurface with three-dimensional models, much more effective

and exhaustive than traditional two-dimensional representations (such as maps and cross-sections).

3D modelling provides a consistent representation of subsurface geology that is essential for improved understanding of subsurface properties and processes. In some application fields, in fact, 3D geological models represent a starting point to realize quantitative models aimed to study and simulate physical processes. Furthermore, by integrating and harmonizing different types of geologic data, the 3D geological models provide integrated information models that may support geoscientists leading with civil engineering, allowing them to optimise the management of infrastructural projects and the geo-hazard assessment during urban land development (Culshaw and Price, 2011).

Different methodologies can be developed to construct 3D models on the base of the complexity of geology and on the type of available geological data (boreholes, outcrops, cross-sections, geological maps, seismic data, etc.) (Kaufmann and Martin, 2009).

The presented 3D model, covering about 64 km^2 of the Rome coastal area, was generated through the integration of multiple geological surface and subsurface datasets. Surface data include a Digital Terrain Model (DTM of the Lazio region at 5x5m resolution, National Geoportal of the Italian Ministry of the Environment) and published geological maps (Funiciello and Giordano, 2008; Giraudi et al., 2009). The surface dataset was integrated with subsurface data available from the literature that ranges in depth from 10 to 100 m, including geological cross-sections (Belluomini et al., 1986; Bellotti et al., 1995, 2007; Capelli et al., 2007; Giraudi et al., 2009; Marra et al., 2013; Milli et al., 2013, 2016; Ciotoli et al., 2016; Salomon et al., 2020), 2D seismic reflection profiles (Bigi et al., 2014) and stratigraphic data from about 1000 boreholes provided by the CNR-IGAG database (URBISIT project funded by Italian Department of Civil Protection – DPC) (Fig. S3).

The 3D model was generated using the 3D Move software package (Midland Valley Ltd.) following different working steps. First, all geological and geophysical data used for the

generation of the 3D model were acquired. Second, the collected data, such as maps, cross-sections and boreholes, were digitized and managed as point, line or polygon layers in a Geographic Information System (GIS) environment. The georeferenced database includes both technical (i.e., depth, elevation, geographic coordinates, anomalies percentage in the case of geochemical dataset) and stratigraphic information. Third, the imported dataset was analysed within the 3D Move software environment. A time/depth conversion, using an average velocity of 1.9 km/sec (Bigi et al., 2014), was applied to the seismic horizons identified in the seismic profiles to correlate them with the geological datasets and to reconstruct the geometry of the detected fault planes.

The fourth step involved the construction of a fence diagram composed of ten regular cross-sections that define the trends of the main stratigraphic units and the fault planes that dissect them. Seven of the reconstructed cross-sections are oriented east-west, perpendicular to the strike of the main fault planes, to better define their 3D geometry. The other cross-sections are oriented northwest-southeast, parallel to the local bedding strike. Geological cross-sections (polyline layer) and boreholes (point layer) were used as input constraints for the generation of the 3D model (fifth step). During this final step, the analyses of the shallow distribution of the soil gas anomalies allowed us to define the main fault planes acting as gas migration pathways and to reconstruct their 3D geometry by following the soil gas anomalies and by correlating the main normal fault planes detected by stratigraphic and geophysical investigations along 2D sections.

The geological surfaces corresponding to fault planes and stratigraphic horizons were modelled using a Delaunay Triangulation function. The model is represented by continuous surfaces that reproduce the geological and structural setting of the area, highlighting the relationship between the main stratigraphic units (highstand and transgressive systems tracts deposits of the TDS and older deposits of the PGS; Fig. S1) and the identified geological structures.

4. Results

4.1. Soil gas distribution and origin

The distribution of the collected soil gas samples is reported in the supplementary figure S2. The figure also shows the locations of the main previous (green stars) (Ciotoli et al., 2013, 2016) and newly recognised gas vents (yellow stars).

Table 1 reports the main statistical parameters of the soil gas and φCO_2 datasets collected in the Ostia Antica and Ponte Galeria areas, south and north of the Tiber river, respectively. The table also shows for comparison the statistical parameters of the soil gas survey conducted in the Fiumicino-Isola Sacra area (Ciotoli et al., 2016), which borders the new surveyed area to the west (Fig. S2).

In the area of Ponte Galeria, CO_2 concentrations and φCO_2 rates range from 0.02 to 13.2 vol.% and from 0.01 to 70.4 g $m^{-2}d^{-1}$, respectively (Fig. S4).

The comparability between means and standard deviations for CO_2 (1.03 and 1.72 vol.%) and φCO_2 (6.8 and 10 g $m^{-2}d^{-1}$) indicates skewed distributions thus suggesting a log-normal distribution for both variables, as shown in the histograms of figures S4a-d. More than 90% of the CO_2 flux data shows values lower than 14.5 g $m^{-2}d^{-1}$, below the background value of the Fiumicino area (20 g $m^{-2}d^{-1}$, Carapezza et al., 2015) and below the normal value linked to the biological activity in the soil (20-30 g $m^{-2}d^{-1}$, Sciarra et al., 2020).

CH_4 concentrations vary between 0.58 and 26.8 ppmv, with a mean of 2.27 ppmv and a standard deviation 2.85 ppmv (Table 1; Fig. S4). These values also indicate a skewed distribution, but not one attributable to a log-normal distribution due to the presence of few outliers (Figs. S4e, f). He concentrations show comparable mean (5.15 ppmv), median (5.14 ppmv) and geometric mean (5.15 ppmv) values (Tab. 1); the concentrations of 90%

of the samples are lower than and/or similar to that of atmospheric air (air = 5.22 ppmv**,** Oliver et al., 1984), while the maximum measured value is 6.44 ppmv.

In the area of Ostia Antica, CO_2 concentrations and φCO_2 rates range from 0.03 to 11.9 vol.% and from 0.32 to 140 g $m^{-2}d^{-1}$, respectively. Also, in this case the similarity between means and standard deviations for CO_2 (2.4 vol.% and 2 vol.%) and φCO_2 (22.3 g $m^{-2}d^{-1}$ and 22.6 g $m^{-2}d^{-1}$), respectively, highlights slightly skewed log-normal statistical distributions (Figs. S4a-d). The upper quartile (30.9 g $m^{-2}d^{-1}$) indicates that 25% of the CO_2 flux data are above the normal value for soil systems.

CH_4 concentrations vary between 0.35 and 12,700 ppmv with a mean of 63.3 ppmv and a standard deviation of 858 ppmv caused by the presence of a few high values (outliers) collected from gas vent zones (Figs. S4e-f). Helium statistical parameters are comparable with those of the Ponte Galeria area, with a maximum measured value of 7.03 ppmv (Table 1).

The comparison of the overall statistics for the Ostia Antica, Ponte Galeria and Fiumicino-Isola Sacra areas indicates that the latter is characterized by very high CO_2 (up to 98%) and CH_4 (up to 37,000 ppmv) soil gas anomalies that occur at localized and/or diffuse degassing zones (i.e., gas vents and/or vent zones with diameter ranging from 1 to 10 m) (Bigi et al, 2014; Ciotoli et al., 2016). Coefficients of variation show the highest variability for CO_2 (237) in the Fiumicino-Isola Sacra, while the highest variability for CH_4 (1357) occurs in the Ostia Antica area (Tab. 1). These statistical results are affected by the discovery of two new gas vents in the Fiumicino-Isola Sacra area (V11 and V12 in Fig. S2), and a new gas vent in the Ostia Antica area (V13 in Fig. S2) during the last survey. At the scale of the used sampling density, gas vents were not discovered in the Ponte Galeria area.

Fiumicino-Isola Sacra and Ostia Antica areas show that 10% of the total φCO_2 rates (43 and 52 g $m^{-2}d^{-1}$, respectively) are higher than the normal value for soil systems (20-30 g $m^{-2}d^{-1}$, Sciarra et al., 2020) (Table 1).

Supplementary figure S5 shows the box-plots of CO_2 and CH_4 concentrations (Figs. S5a, b) and φCO_2 (Fig. S5c) for the three investigated areas. As reported in table 1, the graph confirms that Fiumicino-Isola Sacra and Ostia Antica show very similar median values for all variables, while Ponte Galeria has a lower median for CO_2 and φCO_2 and a slightly higher median value for CH_4 due to the presence of a few outliers and a less skewed distribution.

All data distributions highlight the presence of outliers and extreme values; in particular, Fiumicino-Isola Sacra shows many outliers and extremes linked to the high number of gas vents in this area. Excluding the outliers, the difference between the distribution of CO_2 concentrations and flux between the Fiumicino-Isola Sacra, Ostia Antica and Ponte Galeria could be related to the different soil composition and permeability. The Ostia Antica and Fiumicino-Isola Sacra areas are mainly characterized by beach dune and fluvial sand related to the HST of the TDS (Fig. S1); in contrast, in the Ponte Galeria area, the HST deposits mainly consist of impermeable marsh mud and organic clay that may act as a barrier that prevents gas emission at surface from deeper gas reservoirs (Ciotoli et al., 2016).

Supplementary figure S6 shows the normal probability plots (NPPs) of CO_2, CH_4, and He concentrations for the entire investigated area. Graphs highlight the presence of two statistical populations (background and anomalies) delimited by threshold values: 5% for CO_2, 5 ppmv for CH_4 and 5.5 ppmv for He. These threshold values are used to determine which soil gas concentrations can be linked to a deep source. The value of 30 g $m^{-2}d^{-1}$ is considered as threshold value for the φCO_2 (Sciarra et al., 2020).

Variogram analysis and modelling were conducted to evaluate data autocorrelation structure and estimate the spatial variability of the degassing process. A reliable variogram interpretation and modelling will help to understand the link between the variogram structure and the geological characteristics that influence the soil gas distribution. Experimental variograms are constructed with log-transformed CO_2 concentrations and flux data (supplementary figure S7). Parameters of the variogram models are reported in Table 2.

The variogram of CO_2 concentrations highlights a nested structure composed by an isotropic spherical model with a short range (300 m) and an anisotropic exponential model with the major axis along the NNW-SSE direction and a range of 800m (Fig. S7a). The nested model suggests that CO_2 distribution in soil gas can be attributed to short-scale (i.e., gas vents as spot anomalies) and long-scale (i.e., migration along faults) phenomena. The variogram of CO_2 data constructed along the E-W direction exhibits sinusoidal waves that form peaks and troughs (i.e., hole-effect model) with an inter-peak distance of about 500m (Fig. S7b). This model highlights the cyclicity of the underlying phenomenon, probably linked to the presence of parallel NNW-SSE-trending faults distributed along an E-W direction. The variogram of CO_2 flux data highlights a simple structure consisting of an anisotropic spherical model with a major range of 2200 m along the ENE-WSW direction (Fig. S7c). The parameters of all variogram models are used in the kriging algorithm to construct maps of estimated CO_2 concentrations and flux values at unsampled locations (see section 4.4).

4.2. Gas vent isotopic composition

Table 3 reports molecular and isotopic compositions for gas vents (V) and gas vent zones (s) within the studied area. Most of sampled gas vents have a composition dominated by CO_2 (up to 98.9 vol.%) and very high CH_4 concentrations that range from 0.37 to 3.70

vol.%. Gas vents V11, V12 and V13 were discovered in the new investigated area, while 11s is the only new gas vent zone found. V11 and V12 show a complete isotopic composition analysis ($\delta^{13}C_{CO2}$, $\delta^{13}C_{CH4}$ and $\delta^{2}H_{CH4}$) consistent with those previously published (Ciotoli et al., 2016). Isotopic data are reinterpreted on the basis of new genetic diagrams from Milkov and Etiope (2018) (Fig. 3).

CH_4 isotopic data (Figs. 3a, b) fall within 3 genetic fields: thermogenic, secondary microbial and abiotic. This mixed source is also consistent with previous studies (Ciotoli et al, 2013, 2016; Carapezza et al., 2015). CH_4 concentrations measured at gas vents V11 and V12 have a thermogenic and secondary microbial origin. Figure 3c indicates a mixed origin of the CO_2 (i.e., mantle degassing and/or by thermo-metamorphism of carbonate substratum) in agreement with previous studies (Parisi et al., 2007; Ciotoli et al., 2013, 2016; Carapezza et al., 2015). The new CH_4 values measured at vents V11 and V12 indicate a clear thermogenic origin. A further isotope data graph shows that the processes leading to the production of the observed CH_4 and CO_2 values required formation temperature between 100 and 230 °C (Fig. 3d).

4.3 Spatial distribution and thickness of the POC

POC layers with a thickness ranging between 1 and 3 m are found continuously in the north of the study area, from Le Vignole to the Tiber river (Fig. 4). Boreholes with similar POC thicknesses also occur on the Tiber left bank, in the urbanized Ostia Antica area and extending about 4.5 km to the south-east. Thicker POC layers (from 5 to 8 m) occur locally, such as near the airport (close to a landing strip) and in the area of Stagni di Ostia (south of the Ostia Antica village). Boreholes with POC thicknesses greater than 8m occur on the eastern side of the Fiumicino airport and along the A91 highway in the eastern sector of the investigated area (to the east of the F.sso Galeria, on the right bank of the Tiber river).

The thickest POC layers mainly occur in two sectors of the study area (Fig. 4). The first is located on the north-eastern side of the Fiumicino airport (Ponte Galeria area). POC thickness decreases to the west and southwest, up to the coastline close to the Fiumicino urbanized area. The second sector extends from the Ostia Antica village towards the south, up to the boundary of the "Castel Fusano" park. This sector, which stretches for about 5 km in a NW-SE direction, is bordered to the east and northeast by the outcropping sandy and conglomerate deposits of the coastal environment which represent the inland boundary of the Tiber deltaic body ("Riserva della Macchia" unit; Funiciello and Giordano, 2008) (Fig. 2).

4.4. The structural and stratigraphic setting of the area from the 3D model

The 3D model of the coastal area of Rome is based on an initial fence diagram (Figs. 5 and S8 in the supporting information) constructed via a detailed correlation of several key stratigraphic limits and tectonic structures constrained with well logs, seismic profiles and new and available stratigraphic cross-sections from the literature. Three main stratigraphic surfaces were modelled (from top to bottom): i) the basal surface of the HST of the TDS, corresponding to the maximum flooding surface; ii) the TDS sequence boundary; iii) the basal surface of the PGC deposits (Fig. 6). Integration of the soil gas anomalies within the 3D model constrained the reconstruction of the 3D geometry of the main fault planes recognized in the area (Bigi et al., 2014; Milli et al., 2016). Figure 7 shows the contour map of CO_2 concentrations across the entire investigated area, the locations of the gas vents and the fault planes reconstructed in the 3D model.

The main structural features include NNW-SSE faults that dissect the Pliocene and Pleistocene deposits and are buried under the upper portion of the TDS deposits (Fig. 6). Seismic profiles reported in Bigi et al. (2014) show that the recognized structural elements mainly consist of high angle, SW-dipping normal faults (Fig. S3b).

In the Fiumicino-Isola Sacra area, a 6 km long, NNW-SSE trending, west dipping normal fault (F1) dissects the lower portion of the TDS and the underlying Middle-Upper Pleistocene deposits of the PGS (Figs. 5, 6 and S8, S9 in the supporting information). The F1 fault is clearly visible in the southern sector, where it is also reported both in the seismic profiles of Bigi et al. (2014) and the stratigraphic panels of Milli et al. (2016) (Figs. 2, S1 and S3). Its NNW-SSE trend is indicated by an alignment of small spot anomalies with very high CO_2 concentrations occurring within gas vents (Fig. 7).

Towards the east, the basal unconformity of the TDS is offset by other normal faults (F2 and F4) that are about 8 km in length (Figs. 5, 6 and S8, S9 in the supporting information). These fault planes are sub-parallel to the N-S tract of the Tiber river at the boundary of the Fiumicino-Isola Sacra and Ostia Antica areas and their extension overlaps a cluster of diffuse surface degassing (Fig. 7). Analysis of the seismic profiles highlights a diffuse deformation in correspondence with the F2 and F4 fault planes, as illustrated by the occurrence of small growth folds in their hanging walls. Furthermore, the evidence of small folds in the lower portion of the TDS deposits implies the occurrence of a buried normal fault (F3) between F2 and F4 (Bigi et al., 2014) (Figs. S3, S8, S9).

Other normal faults also cut the basal unconformity of the TDS and the PGS in the Ponte Galeria area (F5, F6 and F7). In the case of fault F6, though soil gas anomalies do not occur in this area (Fig. 7), the correlation between the available stratigraphic cross-sections and the seismic profiles suggests that this fault plane can also be traced northward.

In the easternmost portion of the studied area, two buried normal faults (F8 and F9) were detected in the seismic profiles (Fig. S3); these faults do not offset the TDS sequence boundary but only produce several small folds in the basal unconformity. Their position coincides with local CO_2 anomalies elongated along the E-W course of the Tiber river that do not spread to the south or the north (Fig. 7).

Contour maps of the modelled bottom stratigraphic surfaces (see Fig. 6) show that the Plio-Pleistocene deposits were largely affected by tectonic activity.

In detail, figures 6c and d show that the bottom surfaces of the Pleistocene deposits of the PGS (top surface of the deposits belonging to the Monte Mario Sequence) and the entire TDS deposits deepen to the west due to offset associated with the various dissecting normal faults. Furthermore, the deepening of these deposits close to the fault planes suggests local roll-over anticline geometries as shown by the seismic profiles (Fig. S3).

In the studied area, the basal unconformity of the TDS sequence mainly coincides with the bottom of the TST deposits. The latter, in fact, onlaps directly onto the TDS boundary and only locally on the late LST deposits that, landwards, are only preserved with different thicknesses in correspondence of the Tiber-incised valley (Milli et al., 2016). Therefore, the limited extension of the late low-stand deposits below the present Tiber delta plain does not allow the reconstruction of their top surface and, consequently, the stratigraphic limit between the TST and the late LST deposits.

Figure 6b shows the regular shape of the bottom surface of the HST deposits of the TDS. It deepens progressively toward the west, indicating the possible influence of the substratum geometry on their deposition.

5. Discussion

In this work, new geochemical data are compared, integrated and reinterpreted with previous results obtained in the Fiumicino-Isola Sacra area of the coastal sector of the city of Rome (Ciotoli et al., 2016). Results show that gas emanations occur and are widespread also in the Ostia Antica and Ponte Galeria areas, thus representing an important local geological hazard. The 3D geological reconstruction of the Rome coastal area, based on the integration of surface and subsurface multi-source data available from literature, and the analyses of the thickness of the subsurface peat layers, highlights the

geological factors that control natural and human-induced gas emissions. The spatial distribution of geochemical anomalies provided a useful tool to correlate and trace the faults detected by geological and/or seismic profiles along 2D sections. This information was used to reconstruct the 3D geometry of the main fault planes, thereby highlighting the morphological, structural and stratigraphic features of the area.

The new 3D geological model shows a structural setting dominated by NNW-SSE high-angle normal faults that dip to the south-west (Figs. S8 and S9). This setting is consistent with the structural trend of the regional normal faults system that, together with the coeval NE-SW transverse system, influenced the recent evolution of the Tyrrhenian margin, back-arc basin extension and volcanic activity of the Roman Comagmatic Province (see Acocella and Funiciello, 2006 and references therein).

In this structural scenario, the Tiber river path shows local deviations that may be controlled by the newly reconstructed normal faults. For example, the river tends to align NNW-SSE close to the Ostia Antica village, similar to the trend of the F2, F3 and F4 faults occurring in this area (Fig. 7). Moreover, the E-W orientation of the southern branch of the Tiber river (Fiumara Grande) may also be related to faulting (Marra et al., 2020).

Most of the NNW–SSE normal faults constitute vertical migration pathways for the ascent of deep gases, as illustrated by the presence of aligned multivariable gas anomalies in correspondence with all faults represented in the 3D model, except for fault F6 (Fig. 7). In particular, the maps in figure 7 highlight anisotropic and spot anomalies of CO_2 and ϕCO_2 along the NNW-SSE tract of the Tiber river at the boundary of the Fiumicino-Isola Sacra and Ostia Antica areas. This area is characterized by thin POC layers (i.e., reduced impermeable sedimentary cover) and by the presence of faults (see F2, F3, F4 and F5 faults) that act as main leakage routes for endogenous gases (Figs. 4 and 7).

Small spot anomalies having very high concentrations occur at gas vents located in correspondence with the fault F1. Moreover, very high values of CO_2 concentrations and

flux also occur where the road SR296 crosses the Fiumara Grande and along the SR296 road. Though the geological and structural analyses do not show the presence of structural elements in this zone, the presence of clear and high anisotropically distributed gas anomalies can be linked to a geometrically compatible fault, sub-parallel to those evidenced by the seismic survey.

In the Ostia Antica area (south and west of Ostia Antica village) the absence of subsurface geological data does not allow the identification of fault planes that could explain the shallow soil gas anomalies (Fig. 7). However, the alignment of the spot anomalies of different gas species is compatible with the general structural trend of the area, thus suggesting the potential presence of faults.

The Ponte Galeria area shows the lowest values of CO_2 concentrations and flux (Fig. 7), likely due to the very low permeability of the clay-rich deposits that outcrop locally (i.e., the lacustrine-lagoon and lagoon deposits present in the lower and upper portion of the Ponte Galeria formation, respectively) (Milli et al., 2016). The POC-thickness map supports this hypothesis, as these deposits are thickest (ranging from 2 to more than 10 meters) in the Ponte Galeria area (Fig. 4), thus providing a more effective barrier to gas flow.

Figure 8 shows the contours of CO_2 concentrations and flux higher than 5 vol.% and 30 g $m^{-2}d^{-1}$, respectively. The map also shows classed-post symbols for CH_4 concentrations higher than 5 ppmv (black rhombuses) and He concentrations higher than 5.5 ppmv (green circles), as well as the faults reconstructed in the structural model (dashed blue lines).

This map shows the presence of continuous and/or spot soil gas anomalies (reported as grey bands) that are aligned in a NNW–SSE or ESE-WNW direction (the latter along the Tiber river between Ponte Galeria and the sea). The ESE-WNW trend suggests the probable presence of a “Tiber fault”, not detected along the seismic profiles (Bigi et al., 2014) and therefore not reported in the 3D geological model.

The anisotropic orientation evidenced by the variographic analysis of the CO_2 concentrations and flux data indicates a strong spatial correlation, mainly along the NNW-SSE direction, and confirms the strict link between migration phenomena and the trend of the local faults (supplementary Fig. S7). The presence of recognised parallel structures is also highlighted by the spatial cyclicity showed in the E-W variogram of CO_2 concentrations (supplementary Fig. S7b).

The correlation of the recognized tectonic elements with the course of the Tiber river, also mentioned in previous studies (Ciotoli et al., 2016; Marra et al., 2020), coupled with the presence of soil gas and φCO_2 anomalies at surface, suggests a recent and active deformation along some normal faults, as also indicated by the moderate seismicity that affects the grater Rome area (Ml ranging from 1.5 to 4.7) (Frepoli et al., 2010). The analysis of a seismic profile reported in Bigi et al., 2014 shows that most of the detected normal faults cut the TDS basal unconformity and deform the lower part of the TDS itself, indicating recent tectonic activity during the last 20 kyr. This activity controlled the evolution of the Tiber delta and the deposition of the TDS, as also shown by the geometry of the modelled bottom surfaces reported in figure 6.

Considering the high CO_2 concentrations and flux occurring in the area, we have calculated the potential volume of the emitted CO_2 that could contribute to the budget of present-day non-volcanic greenhouse gases in the atmosphere. After removing the biological flux contribution (i.e., values below 30 g m^{-2} d^{-1}) the total estimated φCO_2 rate originating from vent / diffuse leakage zones (about 3 km^2) is 98.9 t d^{-1} (36,099 t y^{-1}), which represents about 12% of the total CO_2 emission from non-volcanic gas vents in central Italy (about 800 t d^{-1}) as reported in Morner & Etiope, 2002. The calculated CO_2 emission value divided by a total area of about 90 km^2 provides a standardized emission of 402 t y^{-1} km^{-2}.

6. Conclusions

This multi-disciplinary study highlights the geological factors that control the natural and human-induced gas emissions affecting the coastal area of Rome, one of the more important local geological hazards. The comparison of new and previously reported near-surface geochemical data with the structural, lithologic and stratigraphic features of the area, synthetized in a 3D subsurface geological model, highlights: i) the main faults that provide migration pathways for the deep gases towards the surface, and ii) the zones characterized by a sufficiently thick cover of impermeable deposits that seal the subsurface gas accumulations.

High anomalous concentrations of CO_2 (and CH_4) in the soil occur as main gas vents or more diffuse leakage areas along recognised faults and/or in correspondence with thinner impermeable clayey layers. In the urban areas, these gas emissions represent a risk for human health since CO_2 can accumulate in poorly ventilated spaces, such as basements or morphological depressions, and thus reach dangerous concentrations. In contrast, in zones characterized by lower gas anomalies at the surface, due to the presence impermeable deposits, abrupt human-induced degassing can occur during construction activities, such as drilling or different types of underground excavations that cross the impermeable cover or reduce the lithostatic head. Such an event occurred recently during borehole drilling on November 23rd, 2020.

The 3D geological model may help prevent this latter hazard since it provides a detailed reconstruction of the deposits that host the pressurized gas accumulations that may be considered during human activities.

In this work, the shallow distribution of soil gas anomalies was shown to be a useful tool for the elaboration of the 3D geological model since it allowed the detection and delineation of buried faults, which in turn highlighted the influence of these faults on the evolution of the Tiber delta and the course of the Tiber river. The evidence of recent and

active deformation in correspondence of the main fault planes highlights a seismic hazard correlated to the fault segments characterizing the tectonic activity of the Tyrrhenian margin.

With this multidisciplinary approach, we demonstrate that soil gas surveys may be an effective, inexpensive and non-invasive method for locating faults in areas where subsurface geological data are scarce or missing, aiding in the reconstruction of the structural scenario. The newly presented 3D geological model can be directly used to deduce important connections between the subsurface and the natural landscape, as well as recent human activities. Furthermore, the model is useful to better assess the impact of infrastructure on the environment and the gas hazard in the coastal area of Rome.

The presence of strong degassing phenomena makes the coastal area of Rome a case study of the potential contribution of non-volcanic GHG to the present-day atmospheric C-budget. The potential volume of CO_2 emission estimated in this work is of the same order of magnitude as the output calculated for thermal areas in central Italy. The study area also provides an opportunity for to evaluate surface techniques to be used to monitor for potential CO_2 leaks from wells at a Carbon Capture and Storage (CCS) sites, including the associated health risk.

Acknowledgments

This work was conducted in the framework of the VALGO project (FILAS-RU-2014-1120) funded by the Lazio Region and aimed at the assessment of the geological hazards affecting the Ostia Antica area and at the preservation of its cultural heritage.

The research was also funded by Sapienza Università di Roma (Fondi di ricerca di Ateneo 2017).

We would like to thank Prof. Antonio Ciaschi (project leader) and Prof. Luisa Carbone who designed and encouraged the VALGO project.

The Move® software was provided by Midland Valley Exploration Ltd. to the University of Sapienza (Rome) as Academic Software Licensing.

Stan Beaubien is thanked for improvement of the manuscript English.

References

Acocella, V., Funiciello, R., 2006. Transverse systems along the extensional Tyrrhenian margin of central Italy and their influence on volcanism. Tectonics, 25, TC2003.

Barberi, F., Carapezza, M.L., Ranaldi, M., Tarchini, L., 2007. Gas blowout from shallow boreholes at Fiumicino (Rome): Induced hazard and evidence of deep CO2 degassing on the Tyrrhenian margin of Central Italy. Journal of Volcanology and Geothermal Research, 165,17–31.

Bellotti, P., Milli, S., Tortora, P., Valeri, P., 1995. Physical stratigraphy and sedimentology of the late Pleistocene–Holocene Tiber Delta depositional sequence. Sedimentology 42, 617–634.

Bellotti, P., Calderoni, G., Carboni, M.G., Di Bella, L., Tortora, P., Valeri, P., Zernitskaya, V., 2007. Late Quaternary landscape evolution of the Tiber River delta plain (Central Italy): new evidence from pollen data, biostratigraphy and ^{14}C dating. Zeitschrift für Geomorphologie,, 51 4, 505-534.

Belluomini, G., Iuzzolini, P., Manfra, L., Mortari, R., Zalaffi, M., 1986. Evoluzione recente del delta del Tevere. Geologica Romana, 25, 213-224.

Bigi, S., Beaubien, S.E., Ciotoli, G., D'ambrogi, C., Doglioni, C., Ferrante, V., Lombardi, S., Milli, S., Orlando, L., Ruggiero, L., Tartarello, M.C. and Sacco, P., 2014. Mantle derived CO2 migration along active faults within an extensional basin margin (Fiumicino, Rome, Italy). Tectonophysics, 637, 137–149.

Bottinga, Y., 1969. Calculated fractionation factors for carbon and hydrogen isotope exchange in the system calcite-carbon dioxide-graphite-methane-hydrogen-water vapor. Geochimica et Cosmochimica Acta, 33, 1, 49-64.

Calenda, G., Mancini, C.P., Volpi, E., 2005. Distribution of the extreme peak floods of the Tiber River from the XV century. Advances in Water Resources 28, 615–625.

Capelli, G., Mazza, R., Papiccio, C., 2007. Intrusione salina nel Delta del Fiume Tevere. Geologia, idrologia e idrogeologia del settore romano della piana costiera. Giornale di Geologia Applicata 5, 13-28.

Carapezza, M. L., Tarchini, L., Granieri, D., Martelli, M., Gattuso, A., Pagliuca, N., Ranaldi, M., Ricci, T., Grassa, T., Rizzo A., Pizzino, L., Sciarra, A., 2015. Gas blowout from shallow boreholes near Fiumicino International Airport (Rome): Gas origin and hazard assessment, Chemical Geology, 407–408, 54–65.

Carminati, E., Lustrino, M., Doglioni, C., 2012. Geodynamic evolution of the central and western Mediterranean: tectonics vs. igneous petrology constraints. Tectonophysics 579, 173–192.

Catuneanu, O., Galloway, W.E., Kendall, C.G., St, C., Miall, A.D., Posamentier, H.W., Strasser, A. and Tucker, M.E., 2011. Sequence stratigraphy: methodology and nomenclature. Newsletterson Stratigraphy, 44, 173–245.

Ciotoli, G., Etiope, G., Florindo, F., Marra, F., Ruggiero, L., Sauer, P.E., 2013. Sudden deep gas eruption nearby Rome's airport of Fiumicino. Geophysical Research. Letters, 40, 5632-5636.

Ciotoli, G., Etiope, G., Marra, F., Florindo, F., Giraudi, C., Ruggiero, L., 2016. Tiber delta CO_2-CH_4 degassing: A possible hybrid, tectonically active sediment-hosted geothermal system near Rome. Journal Geophysical Research Solid Earth, 121, 48–69.

Culshaw, M.G. and Price, S.J. 2011. The contribution of urban geology to the development, regeneration and conservation of cities. The 2010 Hans Cloos lecture. Bulletin of Engineering Geology and the Environment. 70, 3, 333-376. doi 10.1007/s10064-011-0377-4

Del Ventisette, C., Raspini, F., Ciampalini, A., Di Traglia, F., Moscatelli, M., Pagliaroli, A., Moretti, S., 2015. Use of PSInSAR data to map highly compressible soil layers. Geologica Acta 13, 4, 309–32.

Di Bella, L., Bellotti, P., Frezza, V., Bergamin, L., Carboni, G., 2011. Benthic foraminiferal assemblages of the imperial harbor of Claudius (Rome): Further paleoenvironmental and geoarcheological evidences. The Holocene, 21, 1245-1259.

Faccenna, C., Funiciello, R., Bruni, A., Mattei, M., Sagnotti, L., 1994. Evolution of a transfer related basin: the Ardea basin (Latium, central Italy). Basin Research, 6, 35–46.

Frepoli, A., Marra, F., Maggi, C., Marchetti, A., Nardi, A., Pagliuca, N.M., Pirro, M., 2010. Seismicity, seismogenic structures, and crustal stress fields in the greater Rome area (central Italy). Journal of Geophysical Research 115, B12303.

Funiciello, R., Giordano, G., 2008. La nuova carta geologica di Roma: litostratigrafia e organizzazione stratigrafica. In P.A. Funiciello R., Praturlon A., Giordano G. (Eds). In: La geologia di Roma dal centro storico alla periferia. Memorie Descrittive della Carta geologica d'Italia, 80, 39-85.

Goiran, J.P., Salomon, F., Mazzini, I., Bravard, J.P., Pleuger, E., Vittori, C., Boetto, G., Christiansen, J., Arnaud, P., Pellegrino, A., Pepe, C., Sadori, L., 2014. Geoarchaeology confirms location of the ancient harbour basin of Ostia (Italy). Journal of Archaeological Science. 41. 389–398.

Giraudi, C., Tata, C., Paroli, L., 2009. Late Holocene evolution of Tiber river delta and geoarchaeology of Claudius and Trajan Harbour, Rome. Geoarchaeology 24, 3, 371-382.

Kaufman, O., Martin, T., 2009. Reprint of "3D geological modelling from boreholes, cross-sections and geological maps, application over former natural gas storages in coal mines" [Computers Geosciences, 34 (2008), 3, 278–290]. Computers Geosciences, 35, 70–82.

Lamberti, A., Archetti, R., Kramer, M., Paphitis, D., Mosso, C., Di Risio, M., 2005. European experience of low crested structures for coastal management. Coastal Engineering, 52, 841-866.

Marra, F., Bozzano, F., Cinti, F.R., 2013. Chronostratigraphic and lithologic features of the Tiber River sediments (Rome, Italy): Implications on the post-glacial sea-level rise and Holocene climate. Global and Planetary Change 107,157–176.

Marra, F., Milana, G., Pecchioli, L., Roselli, P., Cangi, G., Famiani, D., Mercuri, A., Carlucci, G., 2020. Historical faulting as the possible cause of earthquake damages in the ancient Roman port city of Ostia. Journal of Seismology, 24, 833–851.

Milkov, A. V., Etiope, G., 2018. Revised genetic diagrams for natural gases based on a global dataset of > 20,000 samples. Organic Geochemistry, 125, 109-120.

Milli, S., D'Ambrogi, C., Bellotti, P., Calderoni, G., Carboni, M.G., Celant, A., Di Bella, L., Di Rita, F., Frezza, V., Magri, D., Pichezzi, R.M., Ricci, V., 2013. The transition from wave-dominated estuary to wave-dominated delta: the Late Quaternary stratigraphic architecture of Tiber River deltaic succession (Italy). Sedimentary Geology, 284–285, 159–180.

Milli, S., Mancini, M., Moscatelli, M., Stigliano, F., Marini, M., Cavinato, G.P., 2016. From river to shelf, anatomy of a high-frequency depositional sequence: the Late Pleistocene to Holocene Tiber depositional sequence. Sedimentology 63, 1886-1928.

Mörner, N. A., Etiope, G., 2002. Carbon degassing from the lithosphere. Global and Planetary Change, 33, 185-203.

Sadori, L., Mazzini, I., Pepe, C., Goiran, J.P., Pleuger, E., Ruscito, V., Salomon, F., Vittori, C., 2016. Palynology and ostracodology at the Roman port of ancient Ostia (Rome, Italy). The Holocene, 26, 1502-1512.

Salomon F., Delile H., Goiran J.P., Bravard J.P., Keay S., 2012. The Canale di Comunicazione Traverso in Portus: the Roman sea harbour under river influence (Tiber delta, Italy). Géomorphologie, 18, 1, 2012, 75-90.

Salomon, F., Vittori, C., Noirot, B., Pleuger, E., Rosa, C., Mazzini, I., Carbonel, P., Djerbi, H., Bellotti, P., Goiran, J.P., 2020. Reconstruction of the Tiber Deltaic stratigraphic successions near Ostia using the PADM chart and tracking of the bedload-derived facies (Rome, Italy). Geomorphology, 365, 107227.

Sciarra, A., Cantucci, B., Sapia, V., De Ritis, R., Ricci, T., Civico, R., Galli, G., Cinti, D., Coltorti, M., 2020. Geochemical and geoelectrical characterization of the Terre Calde di Medolla (Emilia-Romagna, northern Italy) and relations with 2012 seismic sequence. Journal of Geochemical Exploration, 221, 106678.

Sella, P., Billi, A., Mazzini, I., De Filippis, L., Pizzino, L., Sciarra, A., Quattrocchi, F., 2014. A newly-emerged (August 2013) artificially-triggered fumarole near the Fiumicino airport, Rome Italy. Journal of Volcanology and Geothermal Research, 280, 53–66.

Tentori, D., Marsaglia, K.M., Milli, S., 2016. Sand compositional changes as a support for sequence-stratigraphic interpretation: the middle upper Pleistocene to Holocene deposits of the Roman Basin (Rome, Italy). Journal of Sedimentary Research, 86, 10, 1208–1227.

Tentori, D., Milli, S., Marsaglia, K.M., 2018. A source-to-sink compositional model of a present highstand: an example in the low-rank tiber depositional sequence (Latium Tyrrhenian margin, Italy). Journal of Sedimentary Research 88, 10, 1238-1259.

Ventriglia, U., 2002. Geologia del Territorio del Comune di Roma (Amministrazione Provinciale di Roma. Servizio Geologico d'Italia - Carta Geologica d'Italia alla scala 1:100.000, Foglio 150), Roma 2002.

Figure captions

Fig. 1 - (A, B) Key maps illustrating the location of the studied area as well as (C) infrastructure, cultural and environmental sites of interest. Sedimentary environments

(lower and upper delta plain) of the Tiber delta are also shown (modified from Milli et al., 2016).

Figure 2 - (a) Geological map of the coastal area of Rome (Funiciello and Giordano, 2008; Giraudi et al., 2009). (b) Representative cross-section showing the stratigraphic and structural setting of the studied area. Its location is indicated in the geological map. (c) Legend for Figs. 2a,b.

Figure 3 - (a) $\delta^{13}C_{CH4}$ versus $\delta^{2}H_{CH4}$ diagram for the gas discharged within the studied area. (b) Methane/(ethane + propane) ratio versus methane stable carbon isotope composition for the gas released in the investigated area. (c) CO_2 stable carbon isotope composition versus methane stable carbon isotope composition for the gas vents of the studied area. Mature thermogenic gas, OA: oil-associated thermogenic gas; PM: Primary Microbial; A: Abiotic; T: Thermogenic; SM: Secondary Microbial; CR: CO_2 reduction, F: methyl-type fermentation, SM: secondary microbial, EMT: early mature thermogenic gas LMT: late mature thermogenic gas, according to the revised genetic diagrams from Milkov and Etiope (2018). (d) Diagram of $\delta^{13}C$-contents of CO_2 and CH_4 in gas vents together with the isotherms based on theoretical CO_2 - CH_4 fractionation factors (Bottinga, 1969).

Figure 4 - 2D map of the peat and organic clay (POC) layers thicknesses. The analysed boreholes are also indicated.

Figure 5 - Fence diagram showing the main stratigraphic units occurring in the subsurface of the Rome coastal area up to a depth of –100m; from top to bottom: HST deposits of the TDS (in yellow), TST and Late LST deposits of the TDS (in violet), PGS deposits (in brown) and MMS deposits (in pink). The z-axis scale is in meters and is exaggerated by a factor of two. The x- and y-axis coordinate system used is WGS 84/UTM zone 33N. The arrow points north. The lateral extent of the model block is the same represented in figure S3. In figure S1 is reported the legend of the units. In the supporting information we provide a dynamic 3-D view of the fence diagram (Figure S8).

Figure 6 - (a) 3D geological model of the subsurface of the Rome coastal area. The model shows the basal surfaces of (from top to bottom): the HST deposits of the TDS (in yellow); the TST and late LST deposits of the TDS (this surface coincides with TDS sequence

boundary) (in violet), the PGS deposits (this surface coincides with the PGS sequence boundary) (in brown). The z-axis scale is in meters. The x- and y-axis coordinate system used is WGS 84/UTM zone 33N. The lateral extent of the model block is equal to Fig. 5. (b - d). Contour maps of the modelled surfaces and the location of the main fault planes recognized in the area. See figure S1 for an explanation of the units. In the supporting information we provide a dynamic 3-D view of the geological model (Figure S9).

Figure 7 - Contour map of CO_2 concentrations (a) and flux (b) in Fiumicino-Isola Sacra, Ostia Antica and Ponte Galeria areas. Blue dashed lines show the main fault planes (from F1 to F9) that were reconstructed in the 3D model correlating seismic profiles and stratigraphic cross-sections available from literature. Soil gas anomalies were used to trace the fault planes along strike highlighting correlations with the main faults detected by Bigi et al. (2014) and Milli et al. (2016). Green stars indicate gas vents locations.

Figure 8 - The map shows contour areas of CO_2 concentrations and flux higher than 5 vol.% and 30 g $m^{-2}d^{-1}$, respectively, samples with methane higher than 5 ppmv (black rhombuses) and with He higher than 8.5 ppmv (green dots). The map also shows the faults reconstructed in this work (blue dashed lines) and the linear bands of geochemical multi-anomalies (light grey) that indicate the presence of gas emission zones that are potentially linked to new fractured areas.

Table captions:

Table.1 – Soil gas main statistics for the Tiber delta, including the Ponte Galeria, Ostia Antica (this work) and Fiumicino-Isola Sacra urbanized areas (Ciotoli et al., 2016). GM, geometric mean; Min, minimum; Max, maximum; LQ, lower quartile; UQ, upper quartile; 10%, 10th percentile; 90%, 90th percentile; SD, standard deviation.

Table 2 - Parameters of the variogram models used for the construction of the contour maps of estimated carbon dioxide concentration and flux by Ordinary Kriging. Experimental variograms were calculated using log-transformed data. A. Direction, Anisotropy Direction.

Table 3 - Molecular Composition (% v/v) and Isotopic Composition of Stable C (‰, VPDB) and H (‰, VSMOW) of CO_2 and CH_4 in Vents (V) and Soil Gas (s) in the studied areas. bd: below detection limit.

Supplementary material:

Figure S1 - Stratigraphic cross-section showing the depositional architecture of the Tiber Sequence. Its location is indicated in figure 2a. The number of the faults are those reported in the 3D model of figure 6.

Figure S2 - Soil gas distribution in the Ostia Antica and Ponte Galeria (blue dots) and Fiumicino-Isola Sacra (orange dots) areas. Green stars indicate the FGV (Fiumicino Gas Vent) and the location of other gas vents (V1-V10) from Ciotoli et al. (2016), while yellow stars indicate the new gas vents discovered in this work (V11, V12 and V13). Black dots (1s-11s) indicate soil gas vents with very high CH_4 concentration.

Figure S3 - (a) The map shows the geological dataset (cross-sections, seismic profiles and borehole data), available both from the literature and private databases, used to elaborate the 3D model, to analyse the soil gas distribution and to estimate the thickness of peat and organic clay layers in the subsurface; (b) Sketch showing the interpretation of the seismic profiles along the Tiber river from Bigi et al. (2014). The basal unconformity of the TDS and the lower part of the TDS deposits are offset by normal faults, mainly dipping to the west. The number of the faults are those reported in the 3D model of figure 6.

Figure S4 - Multiple frequency histograms of CO_2 concentrations and flux and CH_4 concentrations (normal scale on the left and logarithmic scale on the right). CO_2 concentrations and flux show a log-normal distribution.

Figure S5 - Box-Plots of CO_2 concentrations (a) and flux (b), and CH_4 concentrations (c) measured in the areas of Fiumicino-Isola Sacra (Ciotoli et al., 2016), Ostia Antica and Ponte Galeria (this work). The graph highlights few and low outliers and extreme values for the Ostia Antica and Ponte Galeria, while many and very high outliers and extreme values were measured in Fiumicino-Isola Sacra.

Figure S6 - NPPs for CO_2 (a), CH_4 (b) and He (c) concentrations (% v/v a and ppmv b, c) constructed by using all collected data. The anomaly thresholds were recognized by the slope changes of the curves (5% for CO_2, 5 ppmv for CH_4 and 5.5 ppmv for He).

Figure S7 - Experimental variograms and models calculated for CO_2 concentrations (a-b) and flux (c). Points indicate γ values for the raw data pairs calculated for each lag distance; continuous lines indicate the experimental variogram (black line) and the variogram model (red line). Direction 0.0 corresponds to E-W, direction 20.0 to ENE-WSW and direction 120.0 to NNW-SSE. The model parameters are reported in Table 2.

Figure S8 - Dynamic 3-D view of the fence diagram

Figure S9 - Dynamic 3-D view of the geological model

Table 1

	N	Mean	GM	Media	Min-	LQ	UQ	10%	90%	SD
Ponte Galeria (PG)										
CO_2 (vol.%)	215	1.03	0.58	0.58	0.02-	0.3	0.96	0.17	1.72	1.72
CH_4 (ppmv)	215	2.27	1.84	1.80	0.58-	1.4	2.29	1.03	2.66	2.85
He (ppmv)	163	5.15	5.15	5.14	4.73-	5.0	5.20	5.00	5.30	0.20
ϕCO_2 (g $m^{-2}d^{-1}$)	116	6.79	2.86	3.29	0.01-	1.2	8.98	0.47	14.53	10
Ostia Antica (OA)										
CO_2 (vol.%)	302	2.40	1.64	1.84	0.03	1.0	3.17	0.43	5.00	1.99
CH_4 (ppmv)	219	63.30	1.40	1.13	0.35-	0.8	1.83	0.54	3.10	858
He (ppmv)	181	5.19	5.18	5.18	4.9-	5.1	5.22	5.01	5.32	0.19
ϕCO_2 (g $m^{-2}d^{-1}$)	162	22.26	12.62	14.73	0.32	6.2	30.86	2.54	52.44	22.59
Fiumicino (FIS)										
CO_2 (vol.%)*	1470	4.48	1.59	1.60	0.04	0.6	3.40	0.30	8.20	10.66
CH_4 (ppmv)*	668	397	1.29	1.13	0.1-	0.3	1.87	0.22	3.55	2643
He (ppmv)**	311	5.15	5.12	5.22	1.74-	5.1	5.29	5	5.39	0.48
ϕCO_2 (g $m^{-2}d^{-1}$)***	1035	31.12	12.32	13.35	0.03-	6.6	24.23	3.16	42.89	130.48
All samples										
CO_2 (vol.%)	1987	3.78	1.43	1.40	0.02	0.6	3.10	0.30	6.40	9.28
CH_4 (ppmv)	1102	253.6	1.40	1.33	0.1-	0.5	1.98	0.28	3.10	1963
He (ppmv)	655	5.16	5.14	5.18	1.74-	5.1	5.26	5.00	5.37	0.36
ϕCO^2 (g m^{-2} d^{-1})	1313	27.8	11.0	12.45	0.01-	5.7	23.7	2.34	42.8	116.3

* Ciotoli et al., 2016. * unpublished. *** partially published in Bigi et al., 2014.

Table 2

	Direction	Nugget	Model	Sill	Max Range	Min Range	Anisotropy Ratio	Anisotropy Direction
CO_2	NNW-SSE							
Model 1		0.5	Spherical	0.3	300		1	
Model 2		0.5	Exponential	0.25	800	400	2	120
CO_2	W-E							
Model 1		0.5	Hole Effect	0.35	70		1	0
CO_2 flux	NNW-SSE							
Model 1		0.27	Spherical	0.4	400		1	
Model 2		0.27	Exponential	0.5	1500	750	2	130

Table 3

sample	Site name	Date	CO_2	N_2	O_2	Ar	CH_4	C_2H_6	C_3H_8	$\delta^{13}C_{CO2}$	$\delta^{13}C_{CH4}$	δD
	Ciotoli et al., 2013											
FGV	FGV	ago-13	97.80	1.30			0.90	0.001		-1.1	-48.9	-199
FGVs	FGV soil-gas	ago-13	80.00				0.30	0.002			-38	
V1	V1 (Traiano channel	ago-13	96.20	2.50			1.20	0.002		-1.23	-46.5	-194
V2	V2 (Isola Sacra)	ago-13	96.30	2.80			0.80	0.0005		-0.7	-39.5	-171
V3	V3 (Riding stable soil)	set-13	17.00				2.30	0.0012			-38.8	
V4	V4 (Montini road field)	set-13	4.40				2.50	0.0023			-40.1	
	Ciotoli et al., 2016											
V5	Scafa road Vent	ago-14	98.30				1.70	0.0004	0.0003		-37	
V6	Tiber 1 Vent (Centro Velico)	set-14	98.90				1.02	0.0004	0.0002		-38.5	
V7	Tiber 2 Vent (Centro Velico)	set-14	97.80	1.80			0.37	0.0001	bd	-2.09	-40.2	-162
V8	Tiber 3 Vent (Field)	set-14	97.68	1.57			0.75	0.0002	0.0001	-1.97	-37.2	-163
V9	Tiber 4 Vent (via Col del	set-14	97.46	1.74			0.80	0.0003	0.0002		-40.1	-203
V10	Traiano channel bubbling	set-15					1.95	0.0004	0.0003		-44.9	
1s	Scafa road soil-gas 1	ago-14	9.77	70.84	18.95	0.86	0.08	bd	bd	3.09	-3.2	
2s	Scafa road soil-gas 2	ago-14	29.00		13.30		0.60					
3s	Tiber 2 soil-gas (Field)	set-14	72.00		2.80		0.70				-35	
4s	Tiber 4 (via Arsiero)	set-14	60.00		4.30		0.10				-19	
5s	Tiber 4 (via Arsiero)	set-14	60.62	32.57	6.34	0.39	0.08	bd		-2.38	-18.5	
6s	via dall'Olio soil-gas	set-13	12.20		1.20		1.80					
7s	Traiano Channel soil-gas 1	set-13	58.17	32.52	8.31		0.99	0.0015	0.0008			
8s	Traiano Channel soil-gas 2	set-13	49.40	38.74	11.45		0.40	0.0018	0.0006			
9s	Traiano Channel soil-gas 3	set-13	57.00	34.36	10.47		2.00	0.0003	0.0002			
10s	Sic protected area soil-gas	set-13	3.27	77.90	15.76		3.70					
	This work											
V11	*Traiano channel bubbling*	apr-18	85.87	11.58	1.87		1.15	10.12	bd	-1.84	-48.36	-182
V12	*ASL channel bubbling*	apr-18	89.32	10.13	0.27		0.93	4.74	bd	-1.63	-32.53	-156
V13	*Tiber 2 vent (Dragona)*	apr-18	11.20	79.20	7.80		1.30	0.0005	bd			
11s	*Vicolo Coccia di Morto soil gas*	apr-18	1.02	78.1	19.0		2.12	bd	0.01			

Authors statement

Roberta Maffucci: Conceptualization, Methodology, Investigation, Writing – Original Draft; Giancarlo Ciotoli: Conceptualization, Methodology, Investigation, Writing – Original Draft; Andrea Pietrosante: Investigation, Writing - Review & Editing; Gian Paolo Cavinato: Conceptualization, Methodology, Writing - Review & Editing; Salvatore Milli: Conceptualization, Methodology, Writing - Review & Editing; Livio Ruggiero: Investigation, Writing - Review & Editing; Alessandra Sciarra: Investigation, Writing - Review & Editing; Sabina Bigi: Conceptualization, Methodology, Writing - Review & Editing, Supervision.

Declaration of interests

☒ The authors declare that they have no known competing financial interests or personal relationships that could have appeared to influence the work reported in this paper.

☐The authors declare the following financial interests/personal relationships which may be considered as potential competing interests:

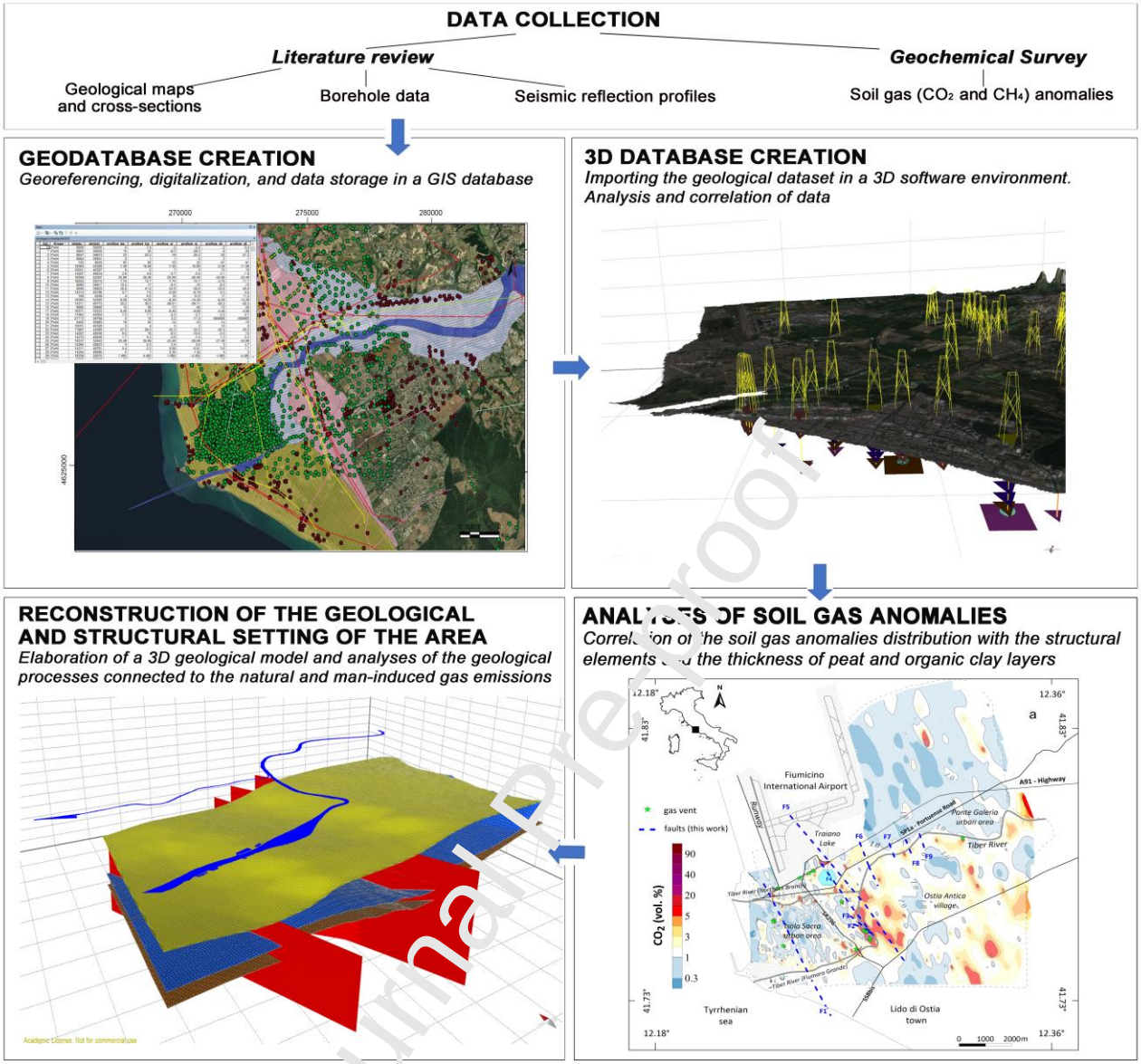

HIGHLIGHTS

- Study approach based on 3D geological modelling and soil gas surveys
- 3D model of the stratigraphic and structural setting of the Rome coastal area
- Identification of areas characterized by soil gas anomalies and controlling factors
- Assessment of the natural and man-induced gas emissions hazards
- Calculation of the volume of CO_2 emission that contributes to the GHG budget